Published in final edited form as:
Nature. ; 478(7370): 502–505. doi:10.1038/nature10535.

Structure and reactivity of a mononuclear non-haem iron(III)–peroxo complex

Jaeheung Cho[1], **Sujin Jeon**[1], **Samuel A. Wilson**[2], **Lei V. Liu**[2], **Eun A Kang**[1], **Joseph J. Braymer**[3], **Mi Hee Lim**[3], **Britt Hedman**[4], **Keith O. Hodgson**[2,4], **Joan Selverstone Valentine**[1,5], **Edward I. Solomon**[2,4], and **Wonwoo Nam**[1]

[1]Department of Bioinspired Science, Department of Chemistry and Nano Science, Center for Biomimetic Systems, Ewha Womans University, Seoul 120-750, Korea.

[2]Department of Chemistry, Stanford University, Stanford, California 94305, USA.

[3]Department of Chemistry and Life Sciences Institute, University of Michigan, Ann Arbor, Michigan 48109, USA.

[4]Stanford Synchrotron Radiation Lightsource, SLAC National Accelerator Laboratory, Stanford University, Menlo Park, California 94025-7015, USA.

[5]Department of Chemistry and Biochemistry, UCLA, Los Angeles, California 90095-1569, USA.

Abstract

Oxygen-containing mononuclear iron species—iron(III)–peroxo, iron(III)–hydroperoxo and iron(IV)–oxo—are key intermediates in the catalytic activation of dioxygen by iron-containing metalloenzymes[1–7]. It has been difficult to generate synthetic analogues of these three active iron–oxygen species in identical host complexes, which is necessary to elucidate changes to the structure of the iron centre during catalysis and the factors that control their chemical reactivities with substrates. Here we report the high-resolution crystal structure of a mononuclear non-haem side-on iron(III)–peroxo complex, $[Fe(III)(TMC)(OO)]^{+}$. We also report a series of chemical reactions in which this iron(III)–peroxo complex is cleanly converted to the iron(III)–hydroperoxo complex, $[Fe(III)(TMC)(OOH)]^{2+}$, via a short-lived intermediate on protonation. This iron(III)–hydroperoxo complex then cleanly converts to the ferryl complex, $[Fe(IV)(TMC)(O)]^{2+}$, via homolytic O–O bond cleavage of the iron(III)–hydroperoxo species. All three of these iron species—the three most biologically relevant iron–oxygen intermediates—have been spectroscopically characterized; we note that they have been obtained using a simple macrocyclic ligand. We have performed relative reactivity studies on these three iron species which reveal that the iron(III)–hydroperoxo complex is the most reactive of the three in the deformylation of aldehydes and that it has a similar reactivity to the iron(IV)–oxo complex in C–H bond activation of alkylaromatics. These reactivity results demonstrate that iron(III)–hydroperoxo species are viable oxidants in both nucleophilic and electrophilic reactions by iron-containing enzymes.

Correspondence and requests for materials should be addressed to J.S.V. (jsv@chem.ucla.edu), E.I.S. (edward.solomon@stanford.edu) or W.N. (wwnam@ewha.ac.kr).

Supplementary Information is linked to the online version of the paper at www.nature.com/nature.

Author Contributions J.C., J.S.V., E.I.S. and W.N. conceived and designed the experiments. J.C., S.J., S.A.W., L.V.L., E.A.K., J.J.B., M.H.L., B.H. and K.O.H. performed the experiments and analysed the data. J.C., S.A.W., L.V.L., J.S.V., E.I.S. and W.N. co-wrote the Letter.

Author Information The crystallographic data for **1** have been deposited with the Cambridge Crystallographic Data Center under accession number CCDC 804038. Reprints and permissions information is available at www.nature.com/reprints. The authors declare no competing financial interests. Readers are welcome to comment on the online version of this article at www.nature.com/nature.

TMC (1,4,8,11-tetramethyl-1,4,8,11-tetraazacyclotetradecane) is a macrocyclic ligand of remarkable versatility in the field of biomimetic chemistry of dioxygen activation by metal complexes. A variety of metal complexes of superoxo, peroxo and oxo ligands showing a wide range of properties have been recently synthesized and characterized using the TMC ligand[8–11]. In the case of iron, TMC complexes of oxo and peroxo ligands are known[11,12]; however, neither the structure of the latter nor that of any other iron(III)–peroxo complexes have been reported before this study. We report here the X-ray crystal structure of a high-spin iron(III)–peroxo complex bearing the TMC ligand, $[Fe(III)(TMC)(OO)]^+$ (**1**; Fig. 1).

The iron(III)–peroxo complex, prepared by reacting $[Fe(II)(TMC)(CF_3SO_3)_2]$ with 5 equiv. H_2O_2 in the presence of 2 equiv. triethylamine in CF_3CH_2OH at 0 °C (ref. 12), was characterized with ultraviolet–visible absorption spectroscopy (Fig. 2a), electrospray ionization mass spectrometry (Supplementary Fig. 1), and electron paramagnetic resonance (EPR) spectroscopy (Supplementary Fig. 2), as reported previously[12], as well as resonance Raman spectroscopy (Supplementary Fig. 3) and X-ray absorption spectroscopy/extended X-ray absorption fine structure (XAS/EXAFS) (Fig. 2b, c). The X-ray crystal structure of **1**–(ClO_4) revealed the mononuclear side-on 1:1 iron complex with O_2; the Fe is in a distorted octahedral geometry, which arises from the triangular FeOO moiety with a small O–Fe–O ('bite') angle of 45.03(17)° (Fig. 1; Supplementary Tables 1 and 2). The FeOO geometry is similar to the crystallographically characterized structure of naphthalene dioxygenase, where dioxygen binds side-on close to the mononuclear iron at the active site (1.75 Å resolution, O–O distance ~1.45 Å)[6]. The structurally determined O–O bond length of 1.463(6) Å in our complex is indicative of peroxo character of the OO group[13], as supported by resonance Raman data[14,15] (Supplementary Figs 3 and 4). It is worth noting that both the O–O bond length and the average Fe–O bond length (1.910 Å) of **1** are longer than those of other metal(III)–peroxo complexes bearing a series of TMC ligands[8–10]. The structure of **1** was further supported by EXAFS analysis (Fig. 2c), which identifies a 2:4 split first shell, with two short Fe–O paths at 1.92 Å and four longer Fe–N TMC paths at ~2.22 Å (Supplementary Table 3, fit 1–3; Supplementary Table 4).

From the structure of **1** (Fig. 1), all four *N*-methyl groups point to the same side of the peroxo moiety, as observed in other metal(III)–peroxo complexes[8–10]. In the case of an iron(IV)–oxo complex bearing the TMC ligand, the *N*-methyl groups of a Sc^{3+}-bound $[Fe(IV)(TMC)(O)]^{2+}$ complex are also *syn* to the oxo ligand[16], whereas those in $[Fe(IV)(TMC)(O)(CH_3CN)]_{2+}$ are *anti* to the oxo ligand[11]. In addition, no axial ligand binds to the iron ion *trans* to the peroxo ligand in **1**, which is different from the $[Fe(IV)(TMC)(O)(CH_3CN)]^{2+}$ complex[11] but similar to other metal(III)–peroxo complexes[8–10] as well as the Sc^{3+}-bound $[Fe(IV)(TMC)(O)]^{2+}$ complex[16].

Addition of a slight excess of $HClO_4$ (for example, 3 equiv. to **1**) to a solution of **1** in acetone/CF_3CH_2OH (3:1) at −40 °C immediately generated a violet intermediate (**2**) with an electronic absorption band at λ_{max} = 526 nm, followed by a conversion ($t_{1/2} \approx 60$ min) from **2** to the corresponding iron(IV)–oxo complex, $[Fe(IV)(TMC)(O)]^{2+}$ (**3**), with an isosbestic point at 735 nm (Fig. 2a; also see Supplementary Fig. 5 for the electrospray ionization mass spectrometry of **3**). (Here λ_{max} is the wavelength of maximum absorption, and $t_{1/2}$ is the half-life.) Intermediate **2** rapidly reverts back to **1** on addition of 3 equiv. tetramethylammonium hydroxide, suggesting that **1** and **2** are interconverted through the previously reported acid-base chemistry between iron(III)–peroxo and iron(III)–hydroperoxo species[14,17,18].

Because the interconversions were fast, the reactions were followed using a stopped-flow spectrometer. On addition of 3 equiv. $HClO_4$ to **1** in acetone/CF_3CH_2OH (3:1) at −40 °C, the absorption band of **1** at λ_{max} = 782 nm disappeared immediately (<2 ms), but the absorption band of **2** at λ_{max} = 526 nm appeared gradually. The full formation of **2** took ~100 ms with an observed rate (k_{obs}) of 93 s^{-1} at −40 °C (Supplementary Fig. 6). These spectral changes indicate that another intermediate (**2'**) exists in the conversion of **1** to **2**, with an extremely fast conversion of **1** to **2'** followed by the relatively slow (that is, ~100 ms) conversion of **2'** to **2** (Fig. 3 and Supplementary Fig. 7). **2'** is likely to be a side-on iron(III)–hydroperoxo species (Fig. 3 and Supplementary Fig. 7), although we have been unable to characterize spectroscopically owing to its extremely short lifetime. The reverse reaction, which is the conversion of **2** to **1**, was also investigated using stopped-flow methods. Addition of 3 equiv. of tetramethylammonium hydroxide to a solution of **2** at −80 °C resulted in the formation of **1** with a clear isosbestic point at 635 nm and a k_{obs} of 19 s^{-1} (Supplementary Fig. 8; see Fig. 3 for reaction pathways).

Intermediate **2** was characterized using a variety of spectroscopic techniques, including EPR, XAS/EXAFS and resonance Raman. The EPR spectrum of a frozen acetone/CF_3CH_2OH (3:1) solution measured at 10 K exhibits signals at g = 6.8, 5.2 and 1.96 (Supplementary Fig. 9), which are indicative of a high-spin (S = 5/2) Fe(III) species[18,19]. The EXAFS data for **2**, compared to **1** (Fig. 2c), also exhibit a distinct shift in the coordination environment, from a 2:4 O:N split first shell in **1** to only a single Fe–O path at a distance of 1.85 Å in **2** (Supplementary Table 3, fit 2-2). This conversion is evident, as a 2:4 split first shell for **2** produces unreasonable bond variances (Supplementary Table 3, fit 2-1). In addition, the remaining Fe–N paths of the TMC ligand have contracted to an average distance of 2.17 Å, reflecting a decrease in ligation. The Fe K-edge of **2** energetically overlays well with that of **1** (Fig. 2b), consistent with the assignment of **2** as a high-spin Fe(III) system. The $1s \rightarrow 3d$ Fe K pre-edge feature of **2** exhibits an increase in pre-edge intensity from 17.5 to 25.6 units, **1** to **2**, respectively (Supplementary Table 5). A pre-edge intensity of 25.6 units is substantially larger then those of other six-coordinate or even five-coordinate complexes[20], thus favouring a five-coordinate structure for **2** (Supplementary Fig. 10).

On 531-nm excitation at 77 K, the resonance Raman spectrum of ^{16}O-labelled **2** in d_6-acetone shows two isotopically sensitive bands at 658 and 868 cm^{-1} (Supplementary Fig. 11). The peak at 658 cm^{-1} shifts to 633 cm^{-1} on ^{18}O-substitution, and is the Fe–O stretch. The peak at 868 cm^{-1} shifts to 820 cm^{-1} on ^{18}O-substitution, and is the O–O stretch. The O–O stretch of **2** is higher than those of other high-spin Fe(III)–OOH(R) complexes (for example, 830 cm^{-1} for $[Fe(H_2bppa)(OOH)]^{2+}$)[19] and is much higher than those of low-spin Fe(III)–OOH(R) complexes (for example, 790 cm^{-1} for $[Fe(N4Py)(OOH)]^{2+}$)[21], consistent with the conclusion that **2** is a high-spin Fe(III)–OOH complex. In addition, the Fe–O stretch of **2** is higher than those of six-coordinate high-spin Fe(III)–OOH(R) complexes (for example, 621 cm^{-1} for $[Fe(H_2bppa)(OOH)]^{2+}$)[19], indicating a stronger Fe–O bond that would be consistent with the absence of a *trans*-axial ligand in **2**. This observation is also consistent with the above XAS results suggesting a five-coordinate model for **2**. These spectroscopic results are further supported by density functional theory calculations that indicate that a high-spin $[Fe(III)(TMC)(OOH)]^{2+}$ complex with its methyl groups oriented *syn* to the OOH^- ligand does not bind a *trans*-axial ligand (Supplementary Fig. 12).

Knowing that an iron(IV)–oxo complex, $[Fe(IV)(TMC)(O)]^{2+}$ (**3**), is formed as the decay product of **2** (Fig. 2; Supplementary Figs 5 and 13), two possible mechanisms of hydroperoxide O–O bond cleavage of **2** are considered: one is the heterolytic O–O bond cleavage of the hydroperoxide ligand of **2**, which would generate an Fe(V)–oxo species, followed by one-electron reduction of the Fe(V)–oxo species that results in the generation of **3** (pathways A and B in Supplementary Fig. 14). The other possibility is the hemolytic hydroperoxide O–O bond cleavage of **2**, affording **3** and a hydroxyl radical (pathway C in Supplementary Fig. 14). Recently, the former mechanism has been proposed[22], based on the observation that the formation rate of **3** from **2** was accelerated by increasing the proton concentration in CH_3CN solution. However, under different solvent conditions, we found no proton concentration effect on the rate of the hydroperoxo O–O bond cleavage of **2**. In fact, the formation rates were essentially the same irrespective of the proton concentration in acetone/CF_3CH_2OH (3:1) and other solvents except CH_3CN (Supplementary Table 6).

Additional evidence that argues against the formation of an iron(V)–oxo species via O–O bond heterolysis was obtained by carrying out reactions in the presence and absence of substrates (Supplementary Fig. 15). If **3** were in fact the product of the one-electron reduction of an iron(V)–oxo species, then the amount of **3** formed in the presence of the substrates should decrease due to fast reactions between the highly reactive iron(V)–oxo species and the substrates (pathways A and D in Supplementary Fig. 14). However, the amounts of **3** formed in the presence and absence of substrates were the same, implying that an iron(V)–oxo species was not generated via an O–O bond heterolysis mechanism in the course of the formation of **3** from **2**. It is also significant that this chemistry, in which a high-spin iron(III)–hydroperoxo species undergoes O–O bond homolysis, has not been reported previously for other high-spin iron(III)–hydroperoxo species[21,23]. A possible reason is that the Fe(IV)=O product in our reaction is an intermediate-spin, six-coordinate complex. Thus, changes along the reaction coordinate in spin state and coordination number could contribute to the energetics of this O–O bond cleavage.

The detailed reactivities of the three intermediates, iron(III)–peroxo (**1**), iron(III)–hydroperoxo (**2**), and iron(IV)–oxo (**3**), have been investigated in both nucleophilic and electrophilic reactions (Fig. 3). The nucleophilic characters of all three intermediates were tested in aldehyde deformylation reactions[24]. On addition of 2-phenylpropionaldehyde (2-PPA) to **1** and **3** in acetone/CF_3CH_2OH (3:1) at −40 °C, the intermediates remained intact without any spectral change (Supplementary Fig. 16). These results indicate that **1** and **3** are relatively unreactive in nucleophilic oxidative reactions at −40 °C, although **1** showed a reactivity with the aldehyde at high temperature (for example, 15 °C)[12]. In contrast, intermediate **2** reacted rapidly with 2-PPA at −40 °C, resulting in the disappearance of its characteristic ultraviolet–visible band. This follows a first-order decay profile and forms **3** with an isosbestic point at 735 nm (Fig. 4a; see Supplementary Fig. 17 for aldehyde concentration effect). The high reactivity of **2** in nucleophilic reactions, compared to the side-on iron(III)–peroxo analogue **1**, is ascribed to the end-on binding mode of the hydroperoxo ligand[24,25] and supported by density functional theory calculations (Supplementary Fig. 18). The reactivity of **2** was further investigated using primary (1°-CHO), secondary (2°-CHO), and tertiary (3°-CHO) aldehydes (Fig. 4b), and the observed reactivity order of 1°-CHO > 2°-CHO > 3°-CHO supports the nucleophilic character of **2** (Supplementary Fig. 19 shows additional evidence for the nucleophilic character of **2**).

The electrophilic characters of **1**, **2** and **3** were also investigated in the oxidation of alkylaromatic compounds with weak C–H bonds, such as xanthene (75.5 kcal mol^{-1}) and 9,10-dihydroanthracene (DHA, 77 kcal mol^{-1}). **1** did not show any significant spectral change on addition of substrates in acetone/CF_3CH_2OH (3:1) at −20 °C (Supplementary Fig. 20a). In contrast, **2** and **3** reacted with DHA under the same conditions (Supplementary Figs 20b and 21a), showing that both **2** and **3** are capable of abstracting a hydrogen atom from DHA and that **2** has a similar reactivity to **3** in this C–H bond activation reaction. Second-order rate constants of 8.1×10^{-1} and 2.4×10^{-2} M^{-1} s^{-1} were determined in the oxidation of xanthene and DHA, respectively, by **2** at −20 °C (Supplementary Fig. 21b). On the basis of the above observations—that the reaction rates are dependent on the substrate concentration and the bond dissociation energies of the substrates (Supplementary Fig. 21b)[26,27]—we conclude that **2** is the active oxidant in abstracting an H atom from the substrates.

In conclusion, iron(III)–hydroperoxo intermediates have been proposed as active oxidants in cytochrome P450-catalysed deformylation of aldehydes[28,29] and activated bleomycin-mediated DNA cleavage via H-atom abstraction[21,30]. We have provided here direct experimental evidence that a high-spin iron(III)–hydroperoxo species is capable of acting as an active oxidant in both nucleophilic and electrophilic reactions.

METHODS SUMMARY

The iron(III)–peroxo complex, $[Fe(III)(TMC)(OO)]^+$ (**1**), was prepared by reacting $[Fe(II)(TMC)(CF_3SO_3)_2]$ with 5 equiv. H_2O_2 in the presence of 2 equiv. triethylamine in CF_3CH_2OH at 0 °C. Unlike the highly unstable nature of **1** in CH_3CN (refs 12, 22), **1** prepared in $CFSCH_2OH$ persisted for several hours at 0 °C, and this greater thermal stability of **1** in alcoholic solvents allowed for the isolation of crystals with ~80% yield, which were used for spectroscopic characterization and reactivity studies. Crystals suitable for structural analysis were obtained from CH_3OH/diethyl ether with excess $NaClO_4$ at −40 °C. See experimental section in Supplementary Information for detailed experimental conditions and procedures, spectroscopic and kinetics analyses, and computational calculations.

Supplementary Material

Refer to Web version on PubMed Central for supplementary material.

Acknowledgments

The work was supported by NRF/MEST of Korea through the CRI (W.N.), the GRL (2010-00353; W.N.), the WCU (R31-2008-000-10010-0; W.N. and J.S.V.) and the 2011 KRICT OASIS Project (W.N.), by NIH grants GM 40392 (E.I.S.) and RR-001209 (K.O.H.), and by NSF grant MCB 0919027 (E.I.S.). J.J.B. acknowledges a Fellowship from NSF EAPSI (OISE-1014685) and the Warner Linfield Award from the University of Michigan. SSRL operations are funded by the Department of Energy (DOE) Office of Science and operated by Stanford University. The SSRL Structural Molecular Biology program is supported by the DOE, Office of Biological and Environmental Research, and by the NIH, National Center for Research Resources, Biomedical Technology Program.

References

1. Solomon EI, et al. Geometric and electronic structure/function correlations in non-heme iron enzymes. Chem. Rev. 2000; 100:235–350. [PubMed: 11749238]
2. Kovaleva EG, Lipscomb JD. Versatility of biological non-heme Fe(II) centers in oxygen activation reactions. Nature Chem. Biol. 2008; 4:186–193. [PubMed: 18277980]
3. Blasiak LC, Vaillancourt FH, Walsh CT, Drennan CL. Crystal structure of the non-haem iron halogenase SyrB2 in syringomycin biosynthesis. Nature. 2006; 440:368–371. [PubMed: 16541079]
4. Rittle J, Green MT. Cytochrome P450 compound I: capture, characterization, and C-H bond activation kinetics. Science. 2010; 330:933–937. [PubMed: 21071661]
5. Kovaleva EG, Lipscomb JD. Crystal structures of Fe^{2+} dioxygenase superoxo, alkylperoxo, and bound product intermediates. Science. 2007; 316:453–457. [PubMed: 17446402]
6. Karlsson A, et al. Crystal structure of naphthalene dioxygenase: side-on binding of dioxygen to iron. Science. 2003; 299:1039–1042. [PubMed: 12586937]
7. Cicchillo RM, et al. An unusual carbon-carbon bond cleavage reaction during phosphinothricin biosynthesis. Nature. 2009; 459:871–874. [PubMed: 19516340]
8. Seo MS, et al. $[Mn(tmc)(O_2)]^+$: a side-on peroxido manganese(III) complex bearing a non-heme ligand. Angew. Chem. Int. Edn. 2007; 46:377–380.
9. Cho J, et al. Synthesis, structural, and spectroscopic characterization and reactivities of mononuclear cobalt(III)-peroxo complexes. J. Am. Chem. Soc. 2010; 132:16977–16986. [PubMed: 21062059]
10. Cho J, et al. Geometric and electronic structure and reactivity of a mononuclear 'side-on' nickel(III)-peroxo complex. Nature Chem. 2009; 1:568–572. [PubMed: 20711413]

11. Rohde J-U, et al. Crystallographic and spectroscopic characterization of a nonheme Fe(IV)=O complex. Science. 2003; 299:1037–1039. [PubMed: 12586936]
12. Annaraj J, Suh Y, Seo MS, Kim SO, Nam W. Mononuclear nonheme ferric-peroxo complex in aldehyde deformylation. Chem. Commun. 2005:4529–4531.
13. Cramer CJ, Tolman WB, Theopold KH, Rheingold AL. Variable character of O-O and M-O bonding in side-on (η^2) 1:1 metal complexes of O_2. Proc. Natl Acad. Sci. USA. 2003; 100:3635–3640. [PubMed: 12634422]
14. Neese F, Solomon EI. Detailed spectroscopic and theoretical studies on $[Fe(EDTA)(O_2)]^{3-}$: electronic structure of the side-on ferric-peroxide bond and its relevance to reactivity. J. Am. Chem. Soc. 1998; 120:12829–12848.
15. Liu J-G, et al. Spectroscopic characterization of a hydroperoxo-heme intermediate: conversion of a side-on peroxo to an end-on hydroperoxo complex. Angew. Chem. Int. Edn. 2009; 48:9262–9267.
16. Fukuzumi S, et al. Crystal structure of a metal ion-bound oxoiron(IV) complex and implications for biological electron transfer. Nature Chem. 2010; 2:756–759. [PubMed: 20729896]
17. Jensen KB, McKenzie CJ, Nielsen LP, Pedersen JZ, Svendsen HM. Deprotonation of low-spin mononuclear iron(III)-hydroperoxide complexes give transient blue species assigned to high-spin iron(III)-peroxide complexes. Chem. Commun. 1999:1313–1314.
18. Simaan AJ, Banse F, Girerd J-J, Wieghardt K, Bill E. The electronic structure of non-heme iron(III)-hydroperoxo and iron(III)-peroxo model complexes studied by Mössbauer and electron paramagnetic resonance spectroscopies. Inorg. Chem. 2001; 40:6538–6540. [PubMed: 11735458]
19. Wada A, et al. Reactivity of hydroperoxide bound to a mononuclear nonheme iron site. Inorg. Chem. 2002; 41:616–618. [PubMed: 11849054]
20. Westre TE, et al. A multiplet analysis of Fe K-edge 1s → 3d pre-edge features of iron complexes. J. Am. Chem. Soc. 1997; 119:6297–6314.
21. Lehnert N, Neese F, Ho RYN, Que L Jr, Solomon EI. Electronic structure and reactivity of low-spin Fe(III)–hydroperoxo complexes: comparison to activated bleomycin. J. Am. Chem. Soc. 2002; 124:10810–10822. [PubMed: 12207537]
22. Li F, et al. Characterization of a high-spin non-heme F^{eIII}-OOH intermediate and its quantitative conversion to an Fe^{IV}=O complex. J. Am. Chem. Soc. 2011; 133:7256–7259. [PubMed: 21517091]
23. Shan X, et al. X-ray absorption spectroscopic studies of high-spin nonheme (alkylperoxo)iron(III) intermediates. Inorg. Chem. 2007; 46:8410–8417. [PubMed: 17764172]
24. Wertz DL, Valentine JS. Nucleophilicity of iron-peroxo porphyrin complexes. Struct. Bonding. 2000; 97:37–60.
25. Selke M, Valentine JS. Switching on the nucleophilic reactivity of a ferric porphyrin peroxo complex. J. Am. Chem. Soc. 1998; 120:2652–2653.
26. Mayer JM. Understanding hydrogen atom transfer: from bond strengths to Marcus theory. Acc. Chem. Res. 2011; 44:36–46. [PubMed: 20977224]
27. Sastri CV, et al. Axial ligand tuning of a nonheme iron(IV)-oxo unit for hydrogen atom abstraction. Proc. Natl Acad. Sci. USA. 2007; 104:19181–19186. [PubMed: 18048327]
28. Vaz ADN, Roberts ES, Coon MJ. Olefin formation in the oxidative deformylation of aldehydes by cytochrome P-450. Mechanistic implications for catalysis by oxygen-derived peroxide. J. Am. Chem. Soc. 1991; 113:5886–5887.
29. Akhtar M, Corina D, Miller S, Shyadehi AZ, Wright JN. Mechanism of the acyl-carbon cleavage and related reactions catalyzed by multifunctional P-450s: studies on cytochrome $P\text{-}450_{17\alpha}$. Biochemistry. 1994; 33:4410–4418. [PubMed: 8155659]
30. Solomon EI, Wong SD, Liu LV, Decker A, Chow MS. Peroxo and oxo intermediates in mononuclear nonheme iron enzymes and related active sites. Curr. Opin. Chem. Biol. 2009; 13:99–113. [PubMed: 19278895]

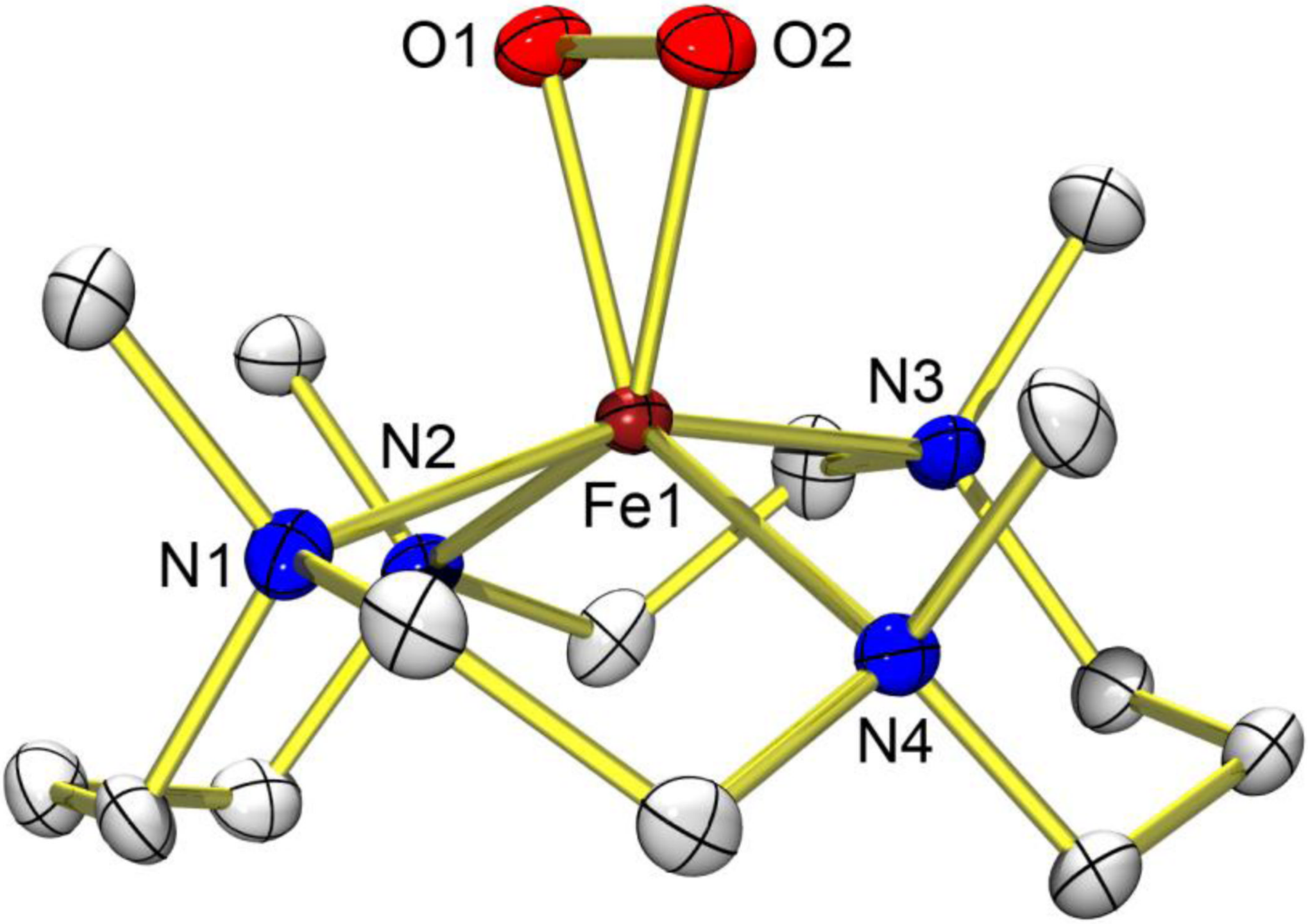

Figure 1. X-ray crystal structure of 1

Structure of $[Fe(TMC)(OO)]^+$ (**1**), with thermal ellipsoids drawn at the 30% probability level, produced using ORTEP software. Hydrogen atoms are omitted for clarity. Selected bond lengths (Å): Fe–O1 1.906(4), Fe–O2 1.914(4), Fe–N1 2.192(4), Fe–N2 2.256(5), Fe–N3 2.180(5), Fe–N4 2.273(4), O1–O2 1.463(6). Selected angles (°): O1–Fe–O2 45.03(17), Fe–O1–O2 67.8(2), Fe–O2–O1 67.2(2).

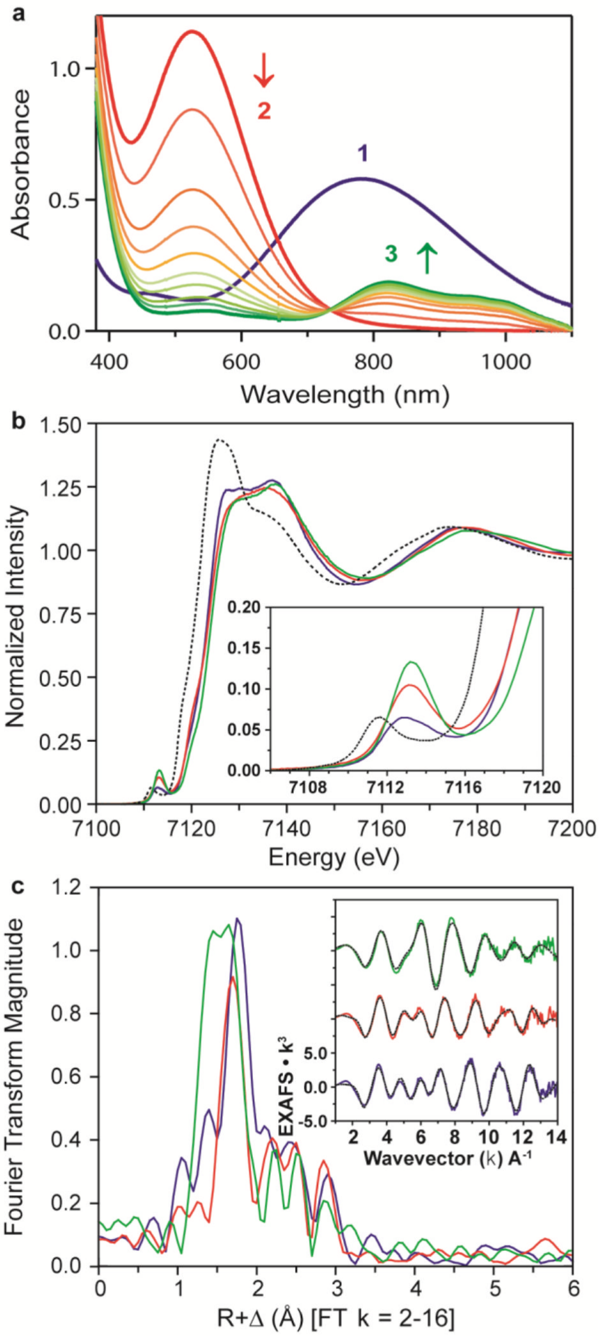

Figure 2. Ultraviolet–visible spectra and XAS data of 1, 2 and 3

In **a–c**, data for **1**, **2** and **3** are shown respectively in blue, red and green. **a**, Ultraviolet–visible spectra of **1**, **2** and **3**; arrows indicate spectral changes for the conversion of **2** to **3** in the reaction of **1** (1 mM) and 3 equiv. $HClO_4$ in acetone/CF_3CH_2OH (3:1) at −40 °C. **b**, Main panel, Fe K-edge XAS data; inset, expanded pre-edge region. Dotted black line shows starting material, high-spin $[Fe(II)(TMC)]^{2+}$, for reference. **c**, Main panel, Fourier transform of EXAFS data (k = 2-16); inset, EXAFS data (solid lines) with final fits (dashed lines). These data show striking differences across the series, most of which are the result of changes to the first coordination sphere.

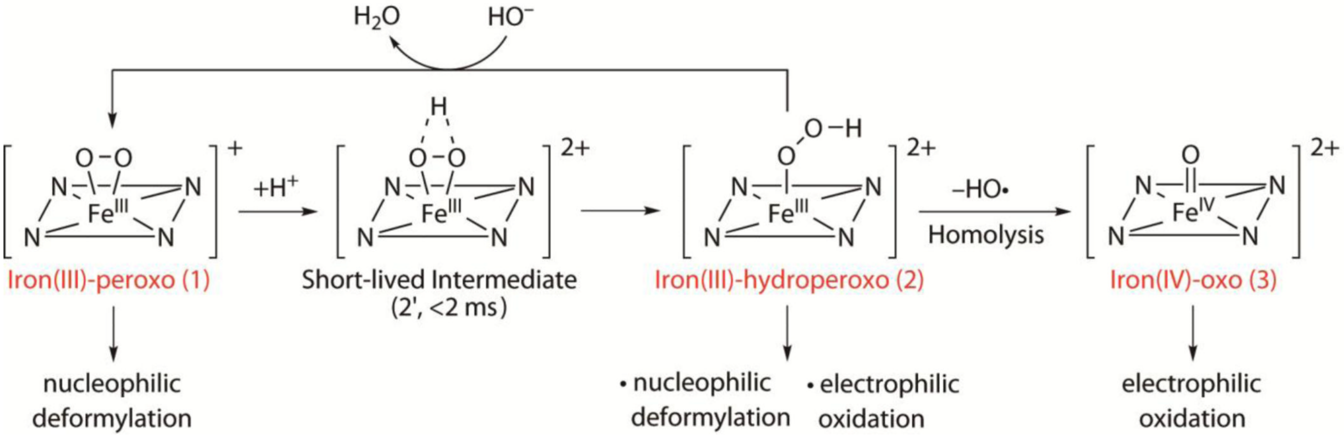

Figure 3. Iron–oxygen intermediates

Generation, structural and spectroscopic characterization, and reactivities of mononuclear non-haem iron–oxygen intermediates detected in the reactivity studies of **1**.

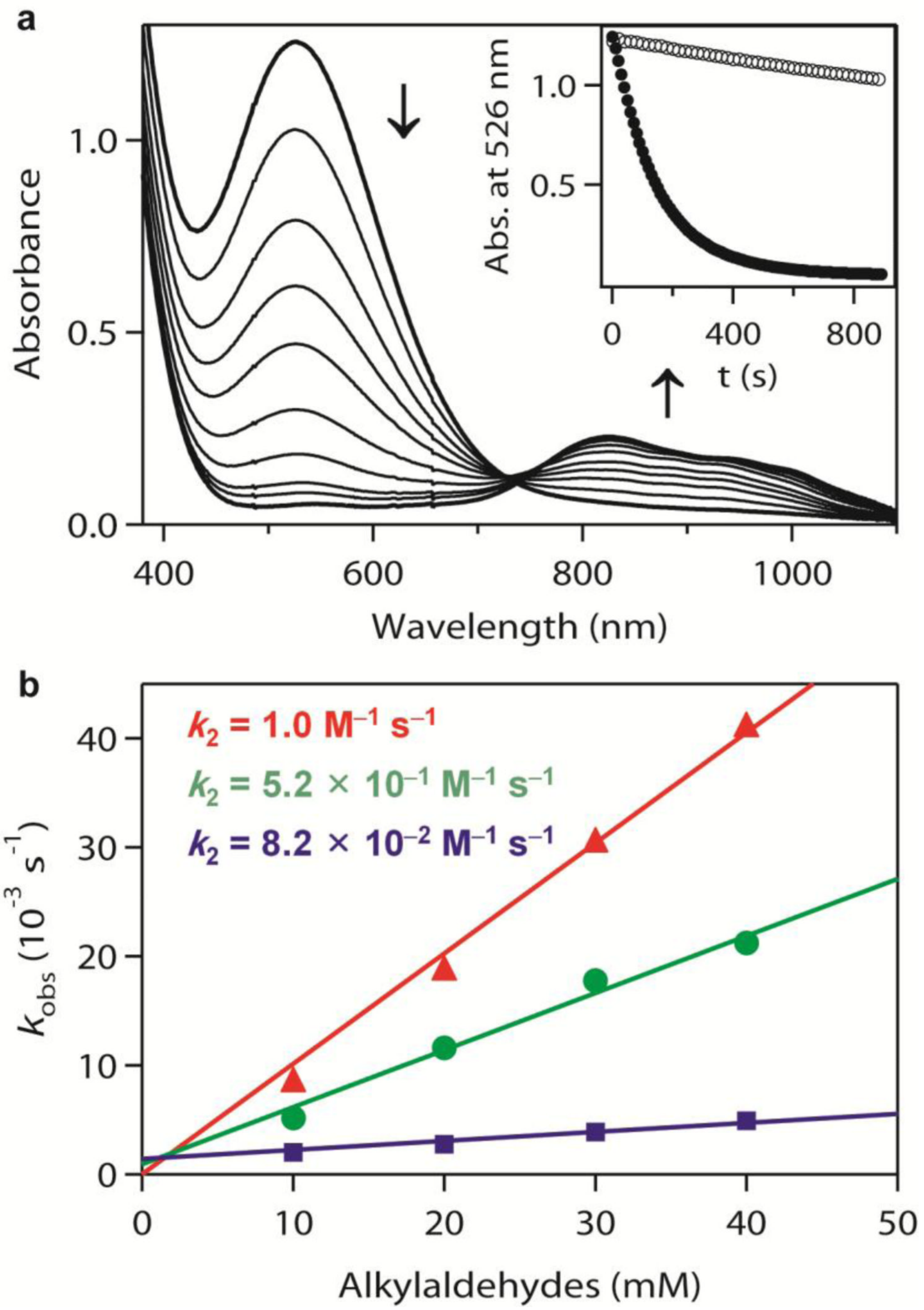

Figure 4. Reactivity studies of 2 with aldehydes

a, Ultraviolet–visible spectral changes showing the decay of **2** (1 mM) and formation of **3** on addition of 2-PPA (50 mM). Inset, time courses of the absorbance change of **2** at 526 nm for the reaction with 2-PPA (filled circles) and for the natural decay (open circles). **b**, Second-order rate constants determined in the reactions of **2** with pentanal (1°-CHO; triangles), 2-methylbutanal (2°-CHO; circles), and pivalaldehyde (3°-CHO; squares). Standard deviation is <10% of the data used in the plot.